Science and Technology Indonesia
e-ISSN:2580-4391 *p*-ISSN:2580-4405
Vol. 11, No. 4, October 2026

Research Paper

Equatorial Electrodynamic Disturbances During the May and October 2024 Extreme Geomagnetic Storms: Implications for HF Communication and Geomagnetically Induced Current Risks in Indonesia

Anwar Santoso[1,2], Sismanto Sismanto[2*], Eddy Hartantyo[2], Rhorom Priyatikanto[1], Nizam Ahmad[3], Clara Yono Yatini[1], Erlansyah[1], Mario Batubara[1], Slamet Supriadi[3], Rizal Suryana[1], Setyanto Cahyo Pranoto[1], Emanuel Sungging Mumpuni[1], Asnawi Husin[1], Mira Juangsih[1], Annis Siradj Mardiani[1]

[1]*Research Center for Space, National Research and Innovation Agency (BRIN), Bandung, West Java, 40173, Indonesia*
[2]*Physics Department, Faculty of Mathematics and Natural Sciences, Gadjah Mada University, Yogyakarta, 55281, Indonesia*
[3]*Research Center for Smart Mechatronics, Research Organization for Electronics and Informatics, BRIN, Bandung, West Java, 40173, Indonesia*
*__Corresponding author__: sismanto@ugm.ac.id

Abstract
The effects of the two biggest storms of Solar Cycle 25, the intense geomagnetic storms of May 10-11 and October 10-11, 2024, on the Indonesian equatorial region are examined in this study. For the 500-kV Jawa-Madura-Bali (JAMALI) transmission network, geomagnetically induced current (GIC) modeling was integrated with magnetometer and ionosonde observations from Pontianak (PTN), close to the geomagnetic equator, and Kupang (KPG), close to the southern crest of the Equatorial Ionization Anomaly (EIA). During both storms, significant equatorial amplification was noted. While the October storm caused lower local perturbations, the horizontal magnetic disturbance at PTN during the May event reached -471 nT, around 16% bigger than the minimum global Dst index (-406 nT). In the JAMALI network, rapid changes in the geomagnetic field produced geoelectric fields that caused quasi-DC currents of 0.6-1.6 A. Such currents may contribute to long-term transformer stress even when they are below essential operational criteria. Significant ionospheric disruptions were caused by both storms, with foF2 reductions of more than 50% and matching drops in maximum usable frequency (MUF) of about 4 MHz, suggesting increased dangers to HF communication equipment. Ionospheric variability over Indonesia is regulated by geomagnetic latitude, local time, storm-time electrodynamic forcing, and thermospheric dynamics, as demonstrated by the differences between PTN and KPG responses.

Keywords
Geomagnetic Storms, Prompt Penetration Electric Fields (PPEF), Geomagnetically Induced Currents (GICs), Ionospheric Storms, Equatorial Electrodynamics

Received: 5 May 2026, Accepted: 3 August 2026
https://doi.org/10.26554/sti.2026.11.4.1448-1463

1. INTRODUCTION

During geomagnetic storms, ionospheric electrodynamics are primarily controlled by two storm-time electric field mechanisms, such as prompt penetration electric field (PPEF) and disturbance dynamo electric field (DDEF). During periods of southward IMF Bz, magnetospheric convection electric fields rapidly penetrate to low and equatorial latitudes, producing PPEF. Recent studies have demonstrated that PPEF dominates the initial phase of geomagnetic storms (Guo et al., 2024; Huang and Zhang, 2021; Fejer et al., 2024). However, the magnitude and duration of PPEF vary considerably with storm intensity, IMF orientation, and longitude, leading to substantial regional differences that remain poorly quantified over Southeast Asia.

At low latitudes, ionospheric electrodynamics are also influenced by DDEF, which originate from thermospheric wind circulation during storms several hours after storm onset. DDEF evolve more slowly as a result of the interaction between storm-induced thermospheric winds, ionospheric currents, and neutral atmosphere dynamics, in contrast to PPEF, which respond rapidly to changes in solar wind-magnetosphere coupling. During the storm recovery phase, their effects are typically manifested as changes to the ambient ionospheric electric field and plasma transport. DDEF contribute to the complex variability seen at equatorial and low latitudes and are a component of the coupled ionosphere- thermosphere response to geomagnetic storms, together with PPEF, thermospheric dynamics, and composition changes. Although DDEF have been extensively investigated, their relative contribution compared with PPEF during successive superstorms remains uncertain, particularly over the Indonesian longitude sector where observations are sparse (Astafyeva et al., 2025; Huang and Zhang, 2021; Fejer et al., 2024).

One of the most significant technological consequences of geomagnetic storms at the Earth's surface is the generation of geomagnetically induced currents (GICs) and disruptions to high-frequency (HF) radio communications. GICs are produced when temporal variations in the geomagnetic field induce geoelectric fields within the electrically conducting Earth, which subsequently drive quasi-DC currents through large-scale technological infrastructures, such as power transmission networks, pipelines, and railway systems (Ahmad et al., 2025; Love et al., 2019). The induced geoelectric field, and consequently the magnitude of GICs, is primarily controlled by the rate of change of the horizontal geomagnetic field (*dX/dt*) (Santoso et al., 2025). Geomagnetically induced currents in power systems may lead to transformer half-cycle saturation, increased demand for reactive power, harmonic distortion, overheating, and even voltage collapse. The most severe GIC impact was the large-scale blackout in Québec during the March 1989 storm (Kappenman and Radasky, 2021). Recent studies have shown that measurable and potentially hazardous GICs can also occur under certain conditions at mid- and low latitudes, particularly as reported by Liu et al. (2014) and Watari et al. (2021). Quantitative assessments of GIC hazards for equatorial power transmission networks are scarce, especially in Southeast Asia, where geomagnetic observations, geoelectric field modelling, and power-grid vulnerability assessments are still limited.

Geomagnetic storms cause significant ionospheric disturbances that are usually described as positive ionospheric storms (when the density or the ratio of O/N_2 increases) or negative ionospheric storms (when the density of electrons or the ratio of O/N_2 decreases) (Aa et al., 2024; Guo et al., 2024). These storm-time ionospheric responses are the result of the complex interaction between storm-time electric fields (PPEF and DDEF), thermospheric circulation, and storm-induced changes in neutral composition. Consequently, the ionospheric response exhibits pronounced spatial and temporal variability. Recent studies have shown that both positive and negative ionospheric storm signatures can occur simultaneously during the 10-11 May 2024 superstorm, depending on longitude, latitude, local time, and the relative contributions of storm-time electrodynamics and thermospheric composition changes (Aa et al., 2024; Astafyeva et al., 2025; Carmo et al., 2024; Tulasi Ram et al., 2024). These contrasting observations indicate that the mechanisms governing regional ionospheric responses remain incompletely understood, particularly over the close-to-equatorial Southeast Asian sector.

Despite recent advances, several important knowledge gaps remain. First, most previous studies have investigated ionospheric disturbances and GICs separately, whereas only a few have examined their coupled responses during the same geomagnetic storm, with a focus on the Indonesian region (~100-115°E), with latitude and longitude spanning from the close to magnetic equator to the southern EIA crest. Second, quantitative assessments of GIC hazards for the 500-kV JAMALI transmission systems, using first-order plane-wave modeling derived from Indonesia's high-resolution magnetometer data, remain scarce. Third, although the severe geomagnetic storms of May and October 2024 have been investigated individually, comparative analyses in geomagnetic and ionospheric responses, and GIC modeling under various storm conditions have not yet been reported. Finally, the influence of latitudinal differences between the region close to the magnetic equator (PTN) and the southern crest of the Equatorial Ionization Anomaly (EIA) (KPG) on regional geomagnetic disturbances and GIC hazards during the severe geomagnetic storms of May 10-11 and October 10-11, 2024 remains poorly understood. To address these knowledge gaps, this study presents a coordinated analysis of two severe geomagnetic storms that occurred on 10-11 May and 10-11 October 2024 using simultaneous geomagnetic and ionospheric observations from the Pontianak (PTN) and Kupang (KPG) observatories. Furthermore, the study evaluates the GIC hazards in the 500-kV Java–Madura–Bali (JAMALI) transmission network using a first-order plane-wave approach and examines the potential implications of the observed ionospheric disturbances for HF radio communication over Indonesia (Nayak et al., 2025; Rout et al., 2025; Santoso et al., 2025). This study is expected to provide new insights into the latitudinal variability of storm-time electrodynamics and its implications for regional GIC hazards and ionospheric disturbances in the Indonesian sector.

2. EXPERIMENTAL SECTION

2.1 Ground Observation Network

This study investigates storm-time geomagnetic and ionospheric responses across two contrasting equatorial electrodynamic regions using observations from two Indonesian geospace observatories, Pontianak (PTN) and Kupang (KPG). PTN and KPG observatories were selected because they offer continuous, high-quality geomagnetic and ionospheric observations and provided complete datasets during the 10-11 May and 10-11 October 2024 geomagnetic storms, whereas comparable simultaneous observations were unavailable or incomplete at other Indonesian observatories. PTN is located close to the magnetic equator (9.30°S MLat, 178.15°W MLon; 0.05°S GLat, 109.08°E GLon), whereas KPG is situated close to the southern crest of the equatorial ionization anomaly (EIA) (18.37°S MLat, 16.66°W MLon; 9.58°S GLat, 123.92°E GLon). In combination with the 500-kV Java-Madura-Bali (JAMALI) transmission network, the north-south configuration of these observatories provides a unique observational framework for investigating the coupled geomagnetic and ionospheric responses together with GICs over the Indonesian sector (Figure 1).

Together, these observatories represent two complementary electrodynamic regimes within the Indonesian low-latitude sector, enabling the investigation of storm-time responses governed by PPEF, DDEF, and thermospheric composition changes. Furthermore, their latitudinal configuration provides an effective observational framework for investigating storm-time geomagnetic and ionospheric variability and the associated impacts on regional geomagnetically induced current (GIC) hazards and high-frequency (HF) radio communication disruptions.

Both observatories are part of the Indonesian geospace monitoring network operated by the National Research and Innovation Agency (BRIN). Each observatory is equipped with an FRG-604-RC triaxial fluxgate magnetometer, which measures three orthogonal geomagnetic field components (X, Y, and Z) were initially recorded at a temporal resolution of 1 second, and a Canadian Advanced Digital Ionosonde (CADI; Controller/Receiver XR-30), which measures the F2-layer critical frequency (foF2) at 15-min intervals. Hourly solar wind parameters, the solar wind speed (Vsw), proton density (Nsw), and dynamic pressure (Psw), including the interplanetary magnetic field (IMF) Bz component, were obtained from the NASA OMNI database. In addition, hourly Dst index values were acquired from the World Data Center for Geomagnetism, Kyoto. These datasets were used to identify and characterize the selected geomagnetic storm events and to support the analysis of geomagnetic and ionospheric responses together with GICs.

2.2 Space Weather Data Acquisition and Processing

The two most intense geomagnetic storms of Solar Cycle 25, the Mother's Day storm of 10-11 May 2024, and the geomagnetic storm of 10-11 October 2024, are the subject of this investigation. Storm-time variations in the horizontal geomagnetic field component (ΔH) observed at PTN and KPG were analyzed to characterize storm-time geomagnetic disturbances. These variations were analyzed together with the Dst index and solar wind parameters (Vsw, Nsw, and Psw) to characterize the solar wind forcing associated with each event. Geomagnetically induced currents (GICs) in the 500-kV Jawa-Madura-Bali (JAMALI) transmission network were estimated using minute-resolution geomagnetic observations and a first-order plane-wave approach, and ionospheric variability and potential implications for high-frequency (HF) communication systems over Indonesia were evaluated by analyzing foF2 observations.

Geomagnetic observations were acquired using FRG-604-RC triaxial fluxgate magnetometers installed at PTN and KPG, which record the three orthogonal geomagnetic field components (X, Y, and Z) at a temporal resolution of 1 second. Before analysis, the geomagnetic data were transformed into the HDZ coordinate system and then averaged per hour for disturbance analysis. The quiet-time baseline (HSq) was calculated using the five International Quiet Days (IQDs) designated by the World Data Center for Geomagnetism, Kyoto. The data were processed using statistical analysis methods. The storm-time horizontal geomagnetic field disturbance, ΔH(t), was quantified using Equation (1):

$$\Delta H(t) = H(t) - HS_q(t) \quad (1)$$

where $H(t)$ is the observed horizontal geomagnetic field component at time t, and $HS_q(t)$ is the monthly quiet-time baseline obtained by averaging the H component over the five International Quiet Days (IQDs) for the corresponding month. The classification of quantity storm refers to Loewe and Prölss (1997).

The above quantity is used as an indicator of the local geomagnetic response. Hourly averages were computed after removing instrument noise and spikes. For both storm periods, ΔH values were compared directly with the provisional Dst index from the World Data Center (WDC) Kyoto to evaluate amplitude differences and timing offsets. Because ΔH alone cannot distinguish the relative contributions of different storm-time electric-field drivers, the *Ey* component of the interplanetary electric field (*IEF-Ey*) was additionally analyzed as a PPEF (Huang et al., 2007; Moges et al., 2022). Additionally, GIC modeling in this study is driven directly by the temporal rate of change of the geomagnetic field (*dX/dt* and *dY/dt*), which captures surface electromagnetic induction effects independently of the local time sector (Zhang et al., 2024; Huang et al., 2025).

Furthermore, the ionospheric data were obtained using Canadian Advanced Digital Ionosondes (CADI), which probe the ionosphere above each observatory by transmitting HF radio waves over the frequency range of 1-20 MHz in 50-kHz increments. Each sounding produces an ionogram every 15 minutes and is then averaged per hour for disturbance analysis, enabling continuous monitoring of the critical frequency (foF2). Ionograms were automatically scaled and manually verified during storm intervals, particularly when spread-F signatures appeared, which can disrupt automatic detection. The percentage foF2 anomaly was calculated using Equation (2), following Ippolito et al. (2020):

$$\delta foF2(\%) = \left(\frac{foF2_{\text{observed}} - foF2_{\text{median}}}{foF2_{\text{median}}}\right) \times 100\% \quad (2)$$

Deviations from the monthly median ($\delta foF2$) were then classified according to ITU-R (2019): minor ($-30 < \delta foF2 <$ 30%), moderate ($-50 < \delta foF2 < 50\%$), severe ($-70\% < \delta foF2 < 70\%$), and extreme ($-70\% > \delta foF2 > 70\%$). In accordance with Huang et al. (2007), the penetration electric field was estimated as 9.6% of IEF-*Ey* to offer a first-order estimate of storm-time PPEF-driven vertical plasma drift. Next, the corresponding vertical drift was computed using $V_{E\times B} = (E\times B)/B^2$, where E is the PPEF-related electric field, and B is the geomagnetic field. Disturbance dynamo electric field effects are not included in this estimation; it solely reflects the PPEF contribution.

Estimation of the electric field (E) and geomagnetically induced currents (GICs) was performed using a first-order plane-wave modeling approach, widely adopted in high- and low-latitude space-weather studies (Horaites et al., 2026). This method assumes that geomagnetic field variations are horizontally uniform over the study region and that the induced electric

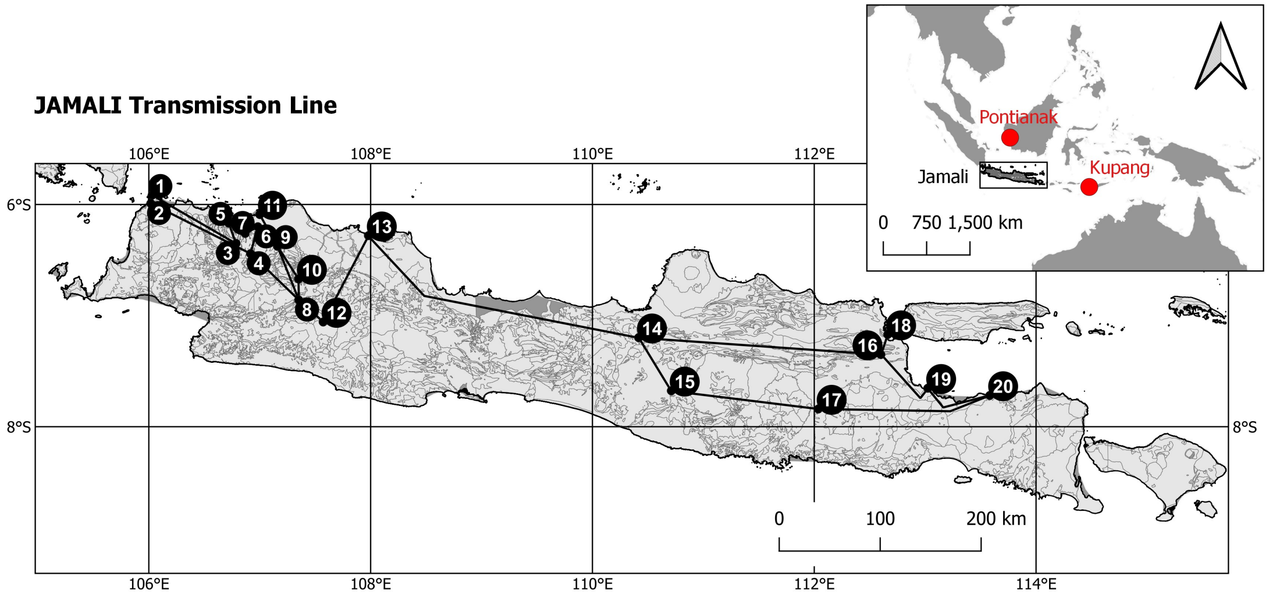

Figure 1. The 500-kV Java–Madura–Bali (JAMALI) Transmission Network Comprising 20 Substations Distributed Across Java, Madura, and Bali. The Network Is Located Approximately 700 km South of PTN and Approximately 1,900 km West of KPG

field is a function of the temporal rate of change of the magnetic field and the effective ground conductivity. Although this simplification neglects local geological heterogeneity and coastal effects, it provides a reasonable first-order estimate of large-scale induction processes in regions such as Indonesia, where detailed conductivity models are not yet available. Although electrical conductivity is known to vary substantially with local geology, incorporating poorly constrained heterogeneous conductivity structures could introduce additional uncertainties into the modeled geoelectric fields. Consequently, the present approach aims to isolate the influence of storm-time geomagnetic field variations (*dB/dt*) on the induced electric field and GIC distribution. Nevertheless, the assumption of uniform conductivity neglects lateral conductivity contrasts that may locally enhance or reduce geoelectric fields. Therefore, the estimated GIC values should be regarded as first-order hazard estimates rather than precise operational predictions. Future studies should incorporate region-specific conductivity models derived from magnetotelluric surveys or three-dimensional conductivity inversions to improve the accuracy of GIC simulations.

Magnetic field data from the PTN and KPG magnetometers were differentiated to obtain the temporal rates of change of the horizontal and declination components, *dX/dt* and *dY/dt*, respectively. The induced geoelectric fields along the north-south (*Ex*) and east-west (*Ey*) directions were then estimated using Equation (3):

$$E_x(t) = \frac{1}{\sqrt{\pi \mu_0 \sigma}} \int_{-\infty}^{t} \frac{g_y(u)}{\sqrt{t-u}} du,\ E_y(t) = -\frac{1}{\sqrt{\pi \mu_0 \sigma}} \int_{-\infty}^{t} \frac{g_x(u)}{\sqrt{t-u}} du \quad (3)$$

where $g_y = dBy/dt$ represents the time derivative of the horizontal geomagnetic field component in the east–west direction (dY/dt), and $g_x = dBx/dt$ represents the time derivative of the horizontal geomagnetic field component in the north–south direction (dX/dt). The variable u denotes the integration time, which begins 10 minutes before time t. Here, μ_0 is the magnetic permeability of free space ($4\pi \times 10^{-7}$ Hm^{-1}) and σ is the ground electrical conductivity. Here, σ is defined as the inverse of the ground resistivity ($\sigma = 1/\rho$, in Ω^{-1} m^{-1}). The adopted resistivity values follow those commonly used for GIC modeling in equatorial regions (Boteler, 2015). For practical implementation, the integration in Equation (3) was initiated 10 minutes before time t and evaluated at 10-minute intervals to estimate the induced geoelectric potential.

The induced electric potential (Vpot) across a transmission-line segment of length L, where LN and LE denote the north-south and east-west distances in km, respectively, was computed using Equation (4) for an ellipsoidal Earth model (Boteler, 2014):

$$V_{pot} = L_N E_x + L_E E_y \quad \text{and} \quad I_{GIC} = \frac{V_{pot}}{R} \quad (4)$$

where R is the effective resistance of the transmission-line-transformer path, including branching (using Kirchhoff's laws for two-, three-, or four-branch nodes), for the 500 kV JAMALI network; representative parameters were used: conductor resistance of about 0.07 Ω/km for ACSR "Zebra" quadruple bundles and a transformer neutral grounding resistance of 0.002 Ω (International Electrotechnical Commission, 2003). This GIC provides a first-order estimate of potential GIC exposure in the JAMALI transmission network. The methodology also allows for the analysis of GIC behavior over time in relation to ΔH fluctuations, linking surface induction processes to storm phases and regional electrical dynamics.

3. RESULTS AND DISCUSSIONS

3.1 Solar Wind Drivers in May and October 2024

On May 9, 2024, at around 16:01 MLT (PTN) and 14:57 MLT (KPG), an interplanetary shock linked to a CME arrival was observed, along with increased solar wind activity and a quick southward swing of IMF Bz to -35.3 nT. On May 11, 2024, at roughly 09:16 MLT (PTN) and 08:12 MLT (KPG), the resultant geomagnetic disturbance attained a minimum Dst of -406 nT. Similar to the previous event, a shock happened on October 9, 2024, at around 08:41 MLT (PTN) and 07:37 MLT (KPG), with IMF Bz hitting -42.2 nT. On October 11, 2024, at roughly 08:16 MLT (PTN) and 07:12 MLT (KPG), the comparable storm attained a minimum Dst of -333 nT. High-resolution solar wind and IMF data from the NASA OMNI database, CME arrival data from the University of Maryland Space Weather Center, and Dst minima from the World Data Center for Geomagnetism, Kyoto, were used to determine shock arrival timeframes.

In accordance with Laundal and Richmond (2017), magnetic local time (MLT) was computed using $MLT = UT + ((\phi - \phi_{sun})/15)$, where ϕ_{sun} is the geomagnetic longitude of the subsolar point and ϕ is the geomagnetic longitude of the observation site. As a result, offsets of roughly 12 minutes for PTN and 16 minutes for KPG are introduced during the conversion from UT to MLT. Table 1 summarizes the CME arrival times for the storms in May and October of 2024, while Table 2 shows the time delays between storm drivers and geomagnetic responses, such as $\Delta T(Bz_{min}\text{-}Dst_{min})$, $\Delta T(Nsw_{max}\text{-}Dst_{min})$, $\Delta T(Vsw_{max}\text{-}Dst_{min})$, and $\Delta T(Psw_{max}\text{-}Dst_{min})$.

3.2 Geomagnetic Responses to the May and October 2024 Storms in the Indonesian Sector

The geomagnetic storms of 10-14 May 2024 and 10-14 October 2024 exhibited extremely intense disturbances, as indicated by a rapid decrease in the Dst index and significant ΔH variations observed at the close-to-equatorial low-latitude station PTN and the low-latitude station KPG, located close to the crest region. During the main phases of both events, sharp variations in Dst, AE, and ΔH at PTN and KPG coincided with enhancements in IEF-*Ey*, reflecting sustained southward orientations of the interplanetary magnetic field (IMF *Bz*) and elevated solar wind speeds. DDEF originate from thermospheric wind-driven dynamo processes and are not directly associated with IEF-*Ey* fluctuations. In contrast, variations in the east-west component of the interplanetary electric field (IEF-*Ey*) indicate changes in solar wind-magnetosphere coupling. They are strongly associated with PPEF activity, which denotes the transmission of magnetospheric convection electric fields into low-latitude regions. PPEF generated by magnetospheric convection electric fields are efficiently transmitted to equatorial and low-latitude ionospheric areas, as demonstrated by their strong temporal coherence.

PPEF associated with geomagnetic storms was distinctly observed during both the initial and main phases. During the May 2024 event, PPEF activity commenced at approximately 23:16 MLT at PTN and 22:12 MLT at KPG on May 10, 2024, with peak intensities recorded at 07:16 MLT (PTN) and 22:12 MLT on 11 May 2024 (KPG). These events predominantly occurred within the midnight-to-morning local time sector, exhibiting peak IEF-Ey amplitudes of approximately 25.75 mV m^{-1}. During the October 2024 event, PPEF activity began at approximately 19:16 MLT at PTN and 18:12 MLT at KPG on 10 October 2024. Peak intensities occurred at 06:16 MLT (PTN) and 05:12 MLT (KPG) on 11 October 2024. In both events, PPEF exhibited significant enhancements in IEF-*Ey*, confirming their association with the penetration of magnetospheric convection electric fields into low latitudes.

Figure 2 presents the horizontal magnetic field (ΔH) difference between PTN (off-equatorial but close to the equatorial) and KPG (off-equatorial), which serves as an essential proxy for evaluating the contribution of equatorial electrodynamics to geomagnetic storms in the Indonesian region. During the main phase in May 2024 (19:16 MLT on May 10, 2024 to 09:16 MLT on May 11, 2024, at PTN and 18:12 on May 10, 2024 to 08:12 MLT on May 11, 2024, at KPG), the ΔH PTN and ΔH KPG events show notable oscillations. During the main phase in October 2024 (21:16 MLT on October 10, 2024, to 08:16 MLT on October 11, 2024, at PTN and 20:12 MLT on October 10, 2024, to 07:12 MLT on October 11, 2024, at KPG), rapid changes were observed. These changes are associated with significant increases in the interplanetary electric field east-west component (IEF-*Ey*), indicating penetration of electric fields induced by PPEF. The results demonstrate that low-latitude geomagnetic disturbances are modulated by PPEF, particularly through rapid temporal variations in the disturbed horizontal geomagnetic field (ΔH), which are associated with enhanced *dX/dt* and *dY/dt* and consequently stronger GIC generation. The main-phase variations are consistent with PPEF-driven electrodynamics. The observed response indicates that the efficiency of PPEF penetration may have fluctuated throughout the storm's evolution, despite elevated IEF-*Ey* levels.

3.3 Induced Electric Fields and GIC Estimates

The rate of change in the horizontal and declination components of the geomagnetic field (dX/dt and dY/dt), E_x and E_y, and AE index, as presented in Figure 3, generated surface electric fields during the geomagnetic storm on May 10-11, 2024, with a ground resistivity (ρ) of 100 $\Omega \cdot$ m. We acknowledge that the assumed uniform ground resistivity influences the absolute magnitude of the estimated GICs through its effect on the calculated geoelectric field. Specifically, lower resistivity values produce larger geoelectric fields and consequently higher GIC estimates, whereas higher resistivity values yield proportionally smaller GIC magnitudes. Nevertheless, because

Table 1. Summary of Solar Wind and Geomagnetic Storm Characteristics Obtained From the GSFC of NASA

Physical Characteristics	10-11 May 2024	10-11 October 2024
Flare class	X2.2	X1.8
Amount of the Flare	2 flares on May 09, 2024, followed by halo CME	single flare on October 09, 2024, followed by halo CME
Travel time to magnetosphere	32 hours	37 hours
Dst minimum	-406 nT	-333 nT
Bz minimum	-35.3 nT	-42.2 nT
$\Delta T\,(Bz_{min}\text{-}Dst_{min})$	2 hours	2 hours
Value of Nsw maximum before Dst reaches minimum	48.1 N. cm^3	31.6 N. cm^3
$\Delta T\,(Nsw_{min}\text{-}Dst_{min})$	6 hours	4 hours
Value of Vsw before Dst reaches minimum	742 km s^{-1}	740 km s^{-1}
$\Delta T\,(Vsw_{max}\text{-}Dst_{min})$	2 hours	9 hours
Psw value when Dstst reaches minimum	55.89 nPa	30.97 nPa
$\Delta T\,(Psw_{max}\text{-}Dst_{min})$	6 hours	9 hours
ΔT_{Dst} onset to minimum	11 hours	11 hours

Table 2. Comparison of Local ΔH Minima With Provisional Dst Values, AE, and IEF-E_y

Physical Characteristics	10-11 May 2024	10-11 October 2024
Flare class	X2.2	X1.8
Dst minimum	-406 nT	-333 nT
Time of Dst Minimum	09:16 MLT (PTN) and (08:12 MLT KPG on May 11, 2024)	08:16 MLT (PTN) and 07:12 MLT (KPG) on October 11, 2024
ΔH minima at PTN	-471 nT	-321 nT
Time of ΔH minima at PTN	16:16 MLT on 11 May 2024	16:16 MLT on 11 October 2024
ΔH minima at KPG	-462 nT	-323 nT
Time of ΔH minima at KPG	15:12 MLT on 11 May 2024	11:12 MLT on 11 October 2024
IEF-E_y maximum	26.19 mV/m	28.95 mV/m
Time of IEF-E_y maxima (MLT PTN)	07:16 MLT on 11 May 2024	06:16 MLT on 11 October 2024
Time of IEF-E_y maxima (MLT KPG)	06:12 MLT on 11 May 2024	05:12 MLT on 11 October 2024
AE index minima	1807 nT	2338 nT
Time of AE minima (MLT PTN)	02:16 MLT on 10 May 2024	23:16 MLT on 10 October 2024
Time of AE minima (MLT KPG)	01:12 MLT on 10 May 2024	22:12 MLT on 10 October 2024

all substations are evaluated under the same conductivity assumption, the relative spatial distribution of GICs and the identification of the most vulnerable substations are expected to remain largely unchanged. These patterns are controlled primarily by the temporal variation of the geomagnetic field (dB/dt) and the transmission network topology rather than by the assumed uniform ground resistivity. The maximum north-south (E_x) and east-west (E_y) fields were approximately $E_x = -57.82$ mV km^{-1} and $E_y = 22.94$ mV km^{-1} (PTN), and $E_x = 35.1$ mV km^{-1} and $E_y = 28.57$ mV km^{-1} (KPG). For the 10-11 October 2024 storm, these rates produced maximum E_x and E_y values of about $E_x = -46.23$ mV km^{-1} and $E_y = -42.83$ mV km^{-1} (PTN), and $E_x = -10.87$ mV km^{-1} and $E_y = -20.93$ mV km^{-1} (KPG).

Figure 3 also shows that GIC peaks are linked to rapid temporal variations in ΔH (large *dY/dt*), rather than the absolute

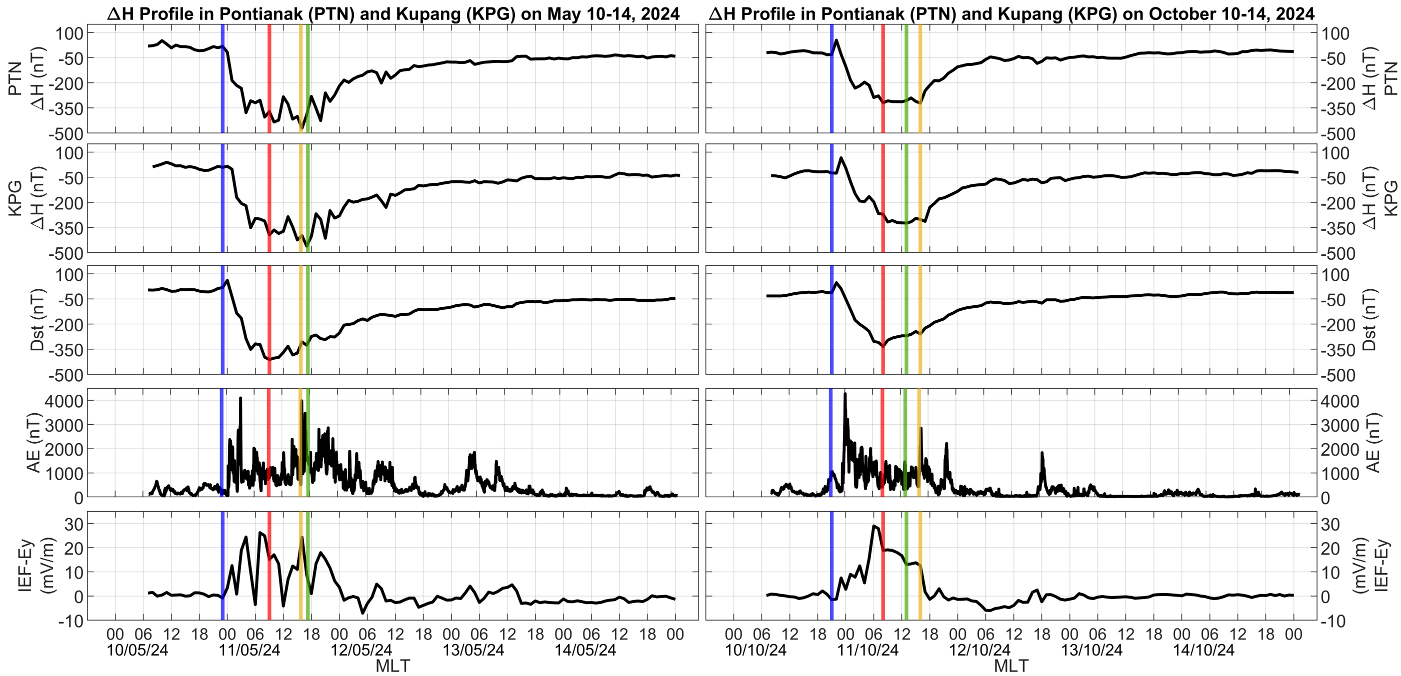

Figure 2. Temporal Variations of ΔH at PTN and KPG During the Geomagnetic Storms of 10-14 May 2024 (Left Panels) and 10-14 October 2024 (Right Panels), Together With the Dst Index, AE Index, and IEF-*Ey*. Storm Onset Is Indicated by Blue Vertical Lines, the Dst Minimum by Red Lines, the Minimum ΔH at PTN by Orange Lines, and the Minimum ΔH at KPG by Green Lines

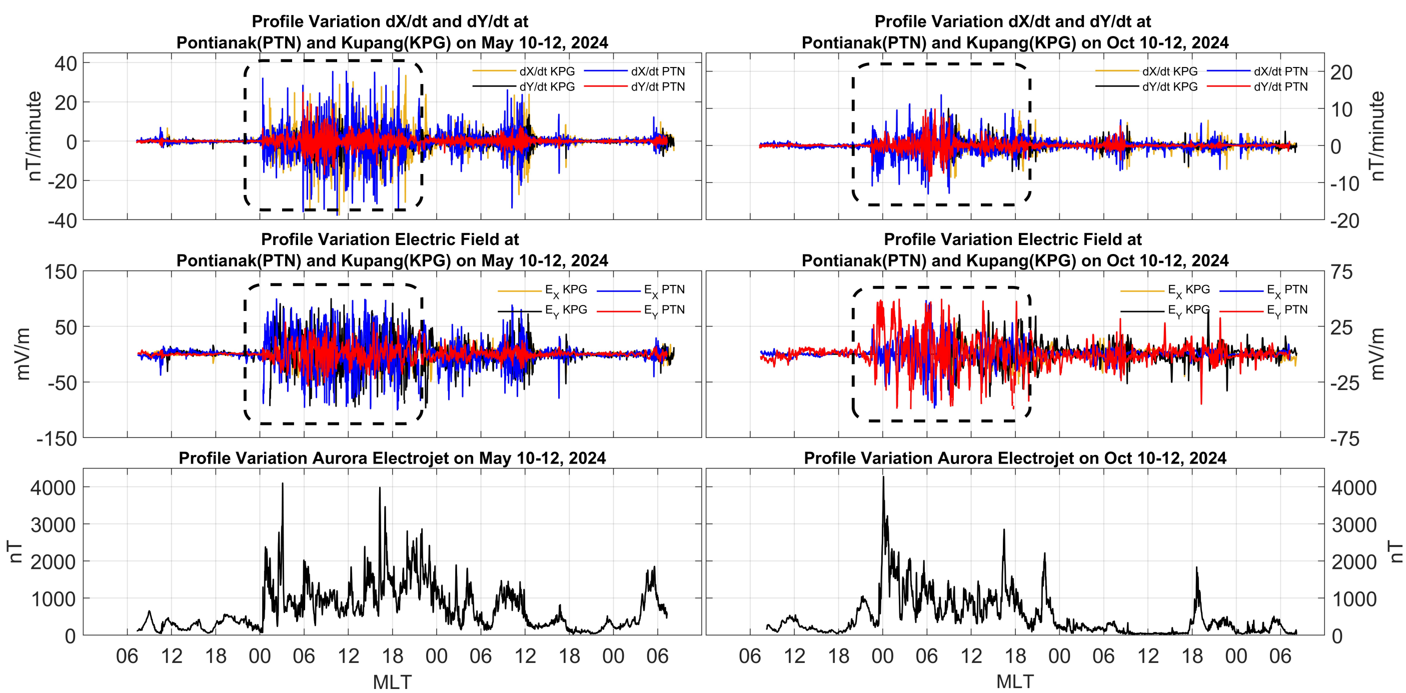

Figure 3. Profiles of dX/dt and dY/dt at PTN and KPG on 10-14 May 2024 (Top Left) and 10-14 October 2024 (Top Right), and Ex and Ey at PTN and KPG on 10-14 May 2024 (Bottom Left) and 10-14 October 2024 (Bottom Right), Together With the AE Index for Both Intervals. Black Dashed Rectangles Mark the Primary Disturbed Intervals Associated With Each Geomagnetic Storm

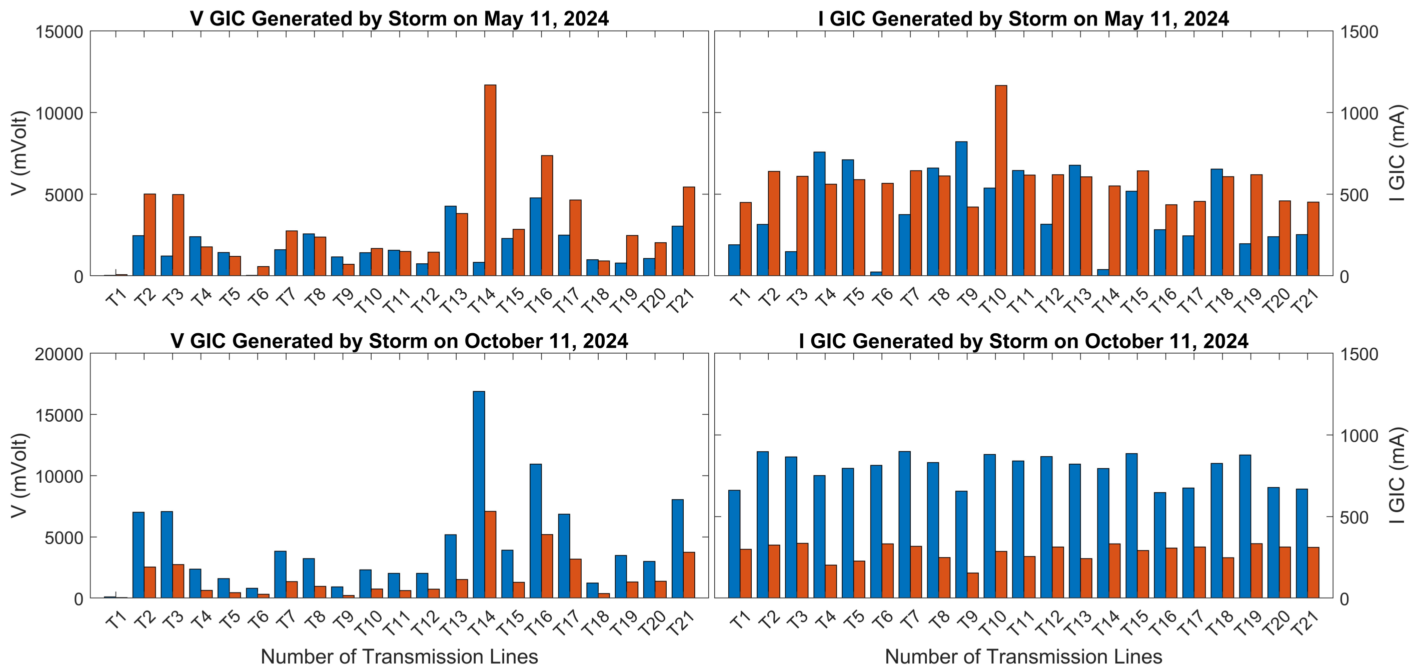

Figure 4. Distribution of Geomagnetically Induced Current (IGIC) and Induced Electric Potential (Vpot) in the JAMALI Transmission Network During the Storms of 10-11 May 2024 (Top Panels) and 10-11 October 2024 (Bottom Panels). Blue Bars Show Estimates Derived From PTN Geomagnetic Data, and Red Bars Show Estimates Derived From KPG Geomagnetic Data

ΔH minima. Rapid PPEF, which result in high gradients in ΔH and increase *dX/dt*, are a significant factor in GIC generation in the equatorial region (Astafyeva et al., 2025). A comparison between the May and October 2024 storms reveals a nonlinear and network-controlled GIC response in the JAMALI 500-kV system. While the magnitude of peak GIC amplitudes was greater during the May storm, the October event caused greater induced voltage across several transmission lines with no corresponding increase in current. This coupled voltage phenomenon illustrates the dominant role of the topology of the power network, the grounding resistance, and the transformer's characteristics in the regulation of GIC amplitude. The results show that, despite moderate disturbance levels, rapid geomagnetic field fluctuations linked to PPEF dynamics can produce measurable GICs even at low latitudes. Although these values are below the typical damage thresholds reported for high-latitude power systems, sustained quasi-DC currents of this magnitude can still contribute to transformer heating, magnetic core saturation, and long-term reactive power oscillations (Kappenman and Radasky, 2021).

To examine these effects within a specific power network, the distribution of geomagnetically induced current (I_{GIC}) discharge through each transformer's neutral grounding resistor in the JAMALI system during both storms is depicted in Figure 4. During the 10-11 May 2024 event, I_{GIC} values at PTN ranged from -0.007 A to 1.4 A, with the maximum occurring at the neutral grounding resistor (R_g) of transformer T8 (R_g8; I_{GIC} = 1.4 A). At KPG, I_{GIC} values ranged from 0.007 A to -1.2 A, with the maximum at T9 (R_g9; $I_{GIC} = -1.2$ A). During the 10-11 October 2024 storm, I_{GIC} values at PTN ranged from -0.002 A to -1.6 A, with the maximum at T1 (R_g1; $I_{GIC} = -1.6$ A). At KPG, values ranged from -0.001 A to -0.6 A, also peaking at T_1 (R_g1; $I_{GIC} = -0.6$ A). Therefore, the estimated GIC magnitudes presented here provide the first quantitative assessment of storm-time GIC hazards in the 500-kV JAMALI transmission network. Comparisons with previous low-latitude studies further indicate that the estimated GIC levels are consistent with those reported for other equatorial and low-latitude power systems (Table 3).

The estimated GIC levels recorded in the JAMALI system are safe and will not cause severe transformer saturation or outages like the 1989 Québec event (Zawawi et al., 2020). The recurring GIC of small magnitude can actually cause false relay activations (due to harmonics), thermal and insulator damage, and increase the demand for reactive power (Kappenman and Radasky, 2021). As the JAMALI corridor develops/outlines the framework for the inter-island high-voltage transmission networking in Indonesia, these space weather impacts will aid in developing/constructing high-voltage corridors. The proposed strategies of deformation of space weather impacts include, in order, real-time GIC monitoring, transformer vulnerability diagnostics, and extreme space weather event planning for critical infrastructure. Taken as a whole, the findings suggest that equatorial regions, particularly as power systems grow and

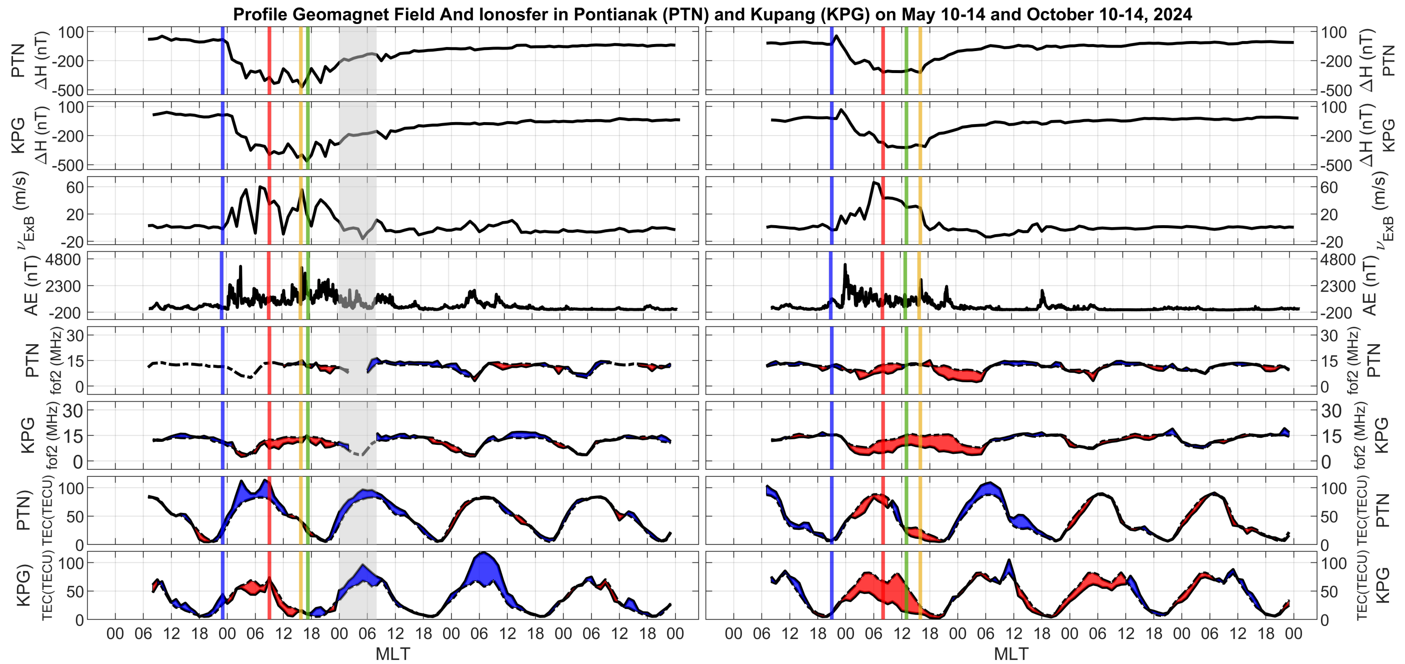

Figure 5. Estimated PPEF-Related Vertical Plasma Drift (VE×B), Δ*H*, AE Index, and the Temporal Variations of foF2 and TEC Together With Their Monthly Medians at PTN and KPG From 10-15 May 2024 (Left Panels) and 10-15 October 2024 (Right Panels). Storm Onset Is Indicated by Blue Vertical Lines, the Dst Minimum by Red Lines, the Minimum Δ*H* at PTN by Orange Lines, and the Minimum Δ*H* at KPG by Green Lines. Shaded Regions Denote Intervals of Spread-F Occurrence

become more connected, do not remain insulated from the impacts of GIC. Therefore, establishing a national magnetotelluric (MT) conductivity database and deploying real-time GIC monitoring at key substations are recommended to strengthen the resilience of Indonesia's critical infrastructure.

To date, no direct GIC measurements have been reported in Indonesia, particularly for the 500-kV Java-Madura-Bali (JAMALI) transmission network. Therefore, the GIC estimates presented in this study are based on a first-order geophysical modeling approach and the associated assumptions adapted from Horaites et al. (2026) and Boteler (2014). Although this approach has been widely adopted in previous GIC studies, the resulting estimates remain subject to several sources of uncertainty arising from the model assumptions, including uncertainties in the calculated geoelectric field components (*Ex* and *Ey*), simplifications in the transmission network topology, and the assumed ground resistivity and transformer grounding resistance. Nevertheless, this first-order approach provides a physically based and practical framework for the preliminary assessment of GIC hazards in the Indonesian power grid until direct GIC measurements become available.

Recent studies have demonstrated that the 10-11 May 2024 Mother's Day geomagnetic storm produced significant space weather effects, especially relate to GIC research at low and equatorial latitudes, although their research objectives differed. Vishnupriya and Manju (2025) assessed GIC risk using *dB/dt* as a proxy without estimating geoelectric fields or GIC magnitudes, whereas Gonzalez-Esparza et al. (2024) reported direct GIC measurements of up to approximately 40 A in the Mexican power grid but did not investigate the associated ionospheric responses. In contrast, the present study provides an integrated assessment of geomagnetic disturbances, ionospheric variability, first-order GIC modeling, and their implications for the Indonesian 500-kV Java–Madura–Bali (JAMALI) transmission network and HF communication systems, thereby offering a more comprehensive evaluation of low-latitude space weather impacts.

3.4 Ionospheric Responses to the May and October 2024 Geomagnetic Storms

The temporal evolution of foF2 (MHz) in relation to its monthly median is shown in Figure 5, together with Δ*H* at PTN and KPG, $V_{E\times B}$, and AE indices between May 10-15, 2024 (left panels) and October 10-15, 2024 (right panels). In accordance with Huang et al. (2007), the parameter $V_{E\times B}$ was computed from the PPEF component approximated as 9.6% of IEF-*Ey* to provide a first-order estimate of storm-time vertical plasma transport. The velocity drift ($V_{E\times B}$) was used to determine the corresponding vertical drift. As a result, the calculated $V_{E\times B}$ should be considered a qualitative measure of storm-time vertical plasma transport since it just represents the PPEF contribution.

Figure 6 illustrates the $\delta foF2(\%)$ during the May 2024 and October 2024 storms. These observations highlight the

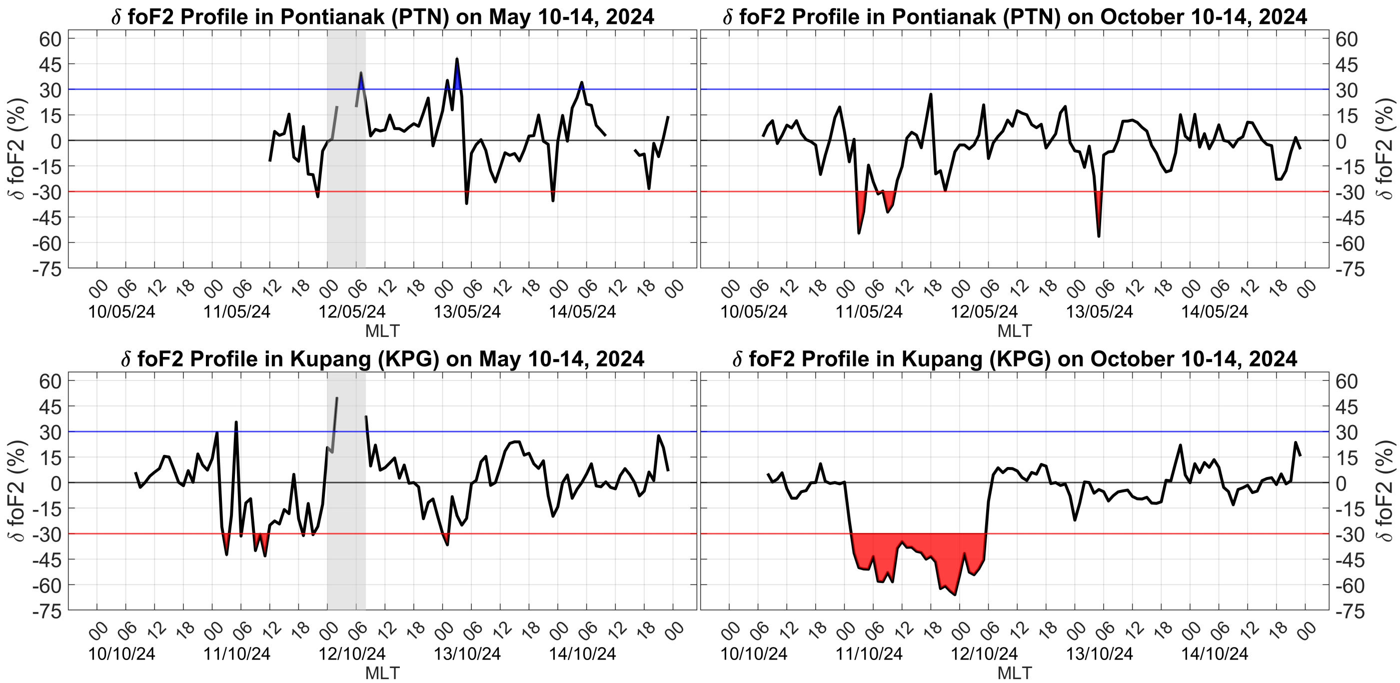

Figure 6. Relative foF2 Deviations (δfoF2) During the Geomagnetic Storms of May 2024 (Left) and October 2024 (Right). Strong Ionospheric Storm Conditions Correspond to |δfoF2| Greater Than 30%, Following Watari et al. (2021). The Blue Horizontal Line Marks the +30% Threshold and the Red Horizontal Line the -30% Threshold. Shaded Regions Denote Intervals of Spread-F Occurrence

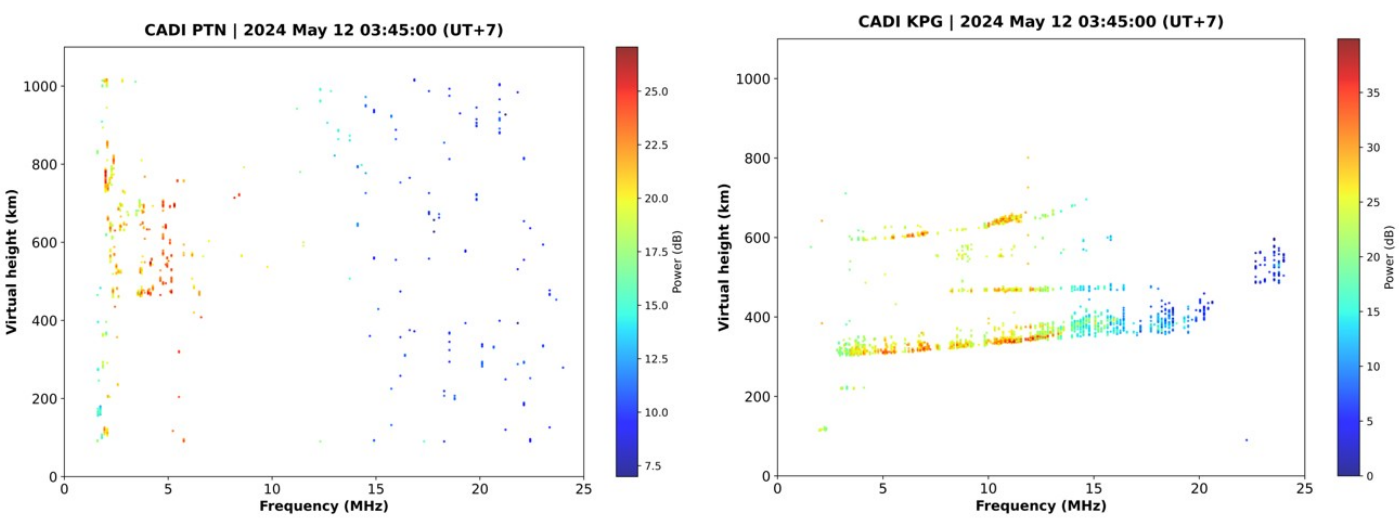

Figure 7. Representative Ionograms Showing Spread-F Signatures During the May 2024 Geomagnetic Storm at (Left-Side) PTN and (Right-Side) KPG

coupled geomagnetic-ionospheric responses associated with two extreme geomagnetic storms over the Indonesian sector. Both events were characterized by alternating negative and positive foF2 phases, indicating large-scale storm-time depletion and redistribution of F-region electron density. The initial foF2 depletions are consistent with the combined influence of storm-time electrodynamic forcing and thermospheric dynamics, including PPEF-driven uplift of F-region plasma, E × B plasma drifts, equatorward-directed neutral winds, and storm-induced changes in thermospheric composition that enhance molecular-to-atomic ratios and increase recombination rates (Balan et al., 2018; Aa et al., 2024; Astafyeva et al., 2025). These mechanisms are well established as the primary drivers of negative ionospheric storms at low and equatorial latitudes.

The storm-time evolution of TEC generally supports the ionospheric behavior inferred from the foF2 observations. During both the May and October 2024 storms, periods of pronounced foF2 depletion were accompanied by corresponding reductions in TEC, indicating that the negative ionospheric storm was associated not only with a decrease in the F2-layer peak electron density but also with a reduction in the total electron content of the ionospheric column. This overall consistency suggests that the storm-time electrodynamic and thermospheric processes affected both the vertical redistribution and the integrated plasma density over the Indonesian sector. The combined foF2 and TEC observations therefore indicate that the storm-time depletion affected both the F2-layer peak density and the integrated plasma content. However, the present dataset does not permit a quantitative separation of these contributions. The stronger and longer-lasting PPEFs during the May 2024 superstorm produced more pronounced plasma uplift and redistribution, resulting in larger simultaneous perturbations in both foF2 and TEC. In contrast, during the October 2024 storm the penetration electric fields were weaker, yet a prolonged negative response was still observed, particularly during the recovery phase, suggesting that storm-time neutral winds and composition changes played a larger role in sustaining the depletion.

The vertical $E \times B$ plasma drift, which is directly influenced by storm-time electric fields, is a crucial mechanism governing these ionospheric responses. During the main phase of geomagnetic storms, strong upward plasma drifts caused by PPEF can elevate the F-region to higher altitudes where recombination rates are lower, increasing electron density at low and middle latitudes. This can cause plasma redistribution, including depletion close to the magnetic equator as a result of upward diffusion and transport. PPEF can cause many uplift events and associated ionospheric variability due to their oscillating structure, which is driven by frequent southward IMF (Bz) excursions.

Furthermore, foF2 observations at PTN during the May 2024 storm are limited, as no data were available during the onset and main phases. However, the available observations during the recovery phase show pronounced negative deviations, with a maximum decrease of approximately -4.93 MHz at 01:16 MLT on 12 May 2024, persisting until about 04:16 MLT. This occurred approximately 16 hours after the peak geomagnetic disturbance, indicating a delayed ionospheric response. Such a delay suggests a combined influence of prompt electrodynamic forcing and subsequent changes in thermospheric composition. foF2 at PTN exhibited a notable positive deviation beginning at 05:16 MLT on 12 May 2024, representing a late recovery-phase enhancement.

The shaded area in Figure 5 (left-side) and Figure 6 (left-side) indicates the time interval of spread-F occurrence (03:16-05:16 MLT on 12 May 2024 at PTN; see also Figure 7a). In contrast, foF2 at KPG shows negative deviations from the median during both the main and recovery phases, with a maximum decrease of approximately -5.66 MHz at 09:12 MLT on 11 May 2024, persisting until about 23:12 MLT. Subsequently, the foF2 response transitions to a positive deviation. The shaded area in Figure 5 (left-side) and Figure 6 (left-side) denotes the occurrence of spread-F (01:12-05:12 MLT on 12 May 2024 at KPG; see also Figure 7b).

For the October 2024 event, foF2 observations at both PTN and KPG capture ionospheric disturbances associated with the storm, primarily during the main and recovery phases, exhibiting broadly similar behavior. The observations show pronounced negative deviations beginning close to storm onset and persisting through the recovery phase until approximately 06:16 MLT on 12 October 2024 at PTN, with a maximum decrease of approximately -6.04 MHz at 03:16 MLT. At KPG, the maximum decrease is approximately -9.51 MHz, observed at 04:12 MLT on 12 October 2024. The maximum negative response occurs approximately 14-15 hours after the peak geomagnetic disturbance, indicating a delayed ionospheric response. This delay suggests a combined influence of prompt electrodynamic forcing and subsequent changes in thermospheric composition.

The substantial modulation of storm-time ionospheric reactions by geomagnetic latitude and local time is emphasized by the different behavior of PTN and KPG. PPEF-related F-region uplift and related $E \times B$ plasma transfer are consistent with the positive foF2 response at PTN during the main phase. The observed foF2 variability at KPG was probably caused by storm-time neutral winds and modification of the Equatorial Ionization Anomaly (EIA). The variations between the two sites demonstrate how intricately thermospheric and electrodynamic processes interact during geomagnetic storms (Bhattacharjee et al., 2025; Shreedevi et al., 2025).

From the onset through the recovery phase of the October 2024 storm, both PTN and KPG exhibited sustained reductions in foF2, characteristic of a prolonged negative ionospheric storm. At PTN, the peak depletion reached approximately -70% (6.04 MHz) at 03:16 MLT on 12 October 2024. At KPG, the maximum decrease was about -66% (9.51 MHz), occurring at 23:12 MLT on 11 October 2024. The ionospheric response at both stations was initially dominated by negative disturbances associated with $E \times B$ plasma drifts and PPEF. However, during the recovery phase, storm-time neutral winds and coupling with the equatorial ionization anomaly (EIA) became the dominant factors sustaining the prolonged negative response. The more pronounced and persistent decline in foF2 at KPG suggests that low-latitude regions close to the EIA crest are more sensitive to thermospheric composition changes than locations closer to the magnetic equator. From an operational perspective, a reduction in foF2 of approximately 50% (corresponding to ~4 MHz) sustained over several hours indicates a high likelihood of HF communication disruptions along equatorial aviation and maritime routes. A combination of neutral wind circulation, thermospheric composition changes, and storm-time electrodynamic force is probably responsible for the extended negative storm phase. Nevertheless, straightforward separation of the proportional contributions

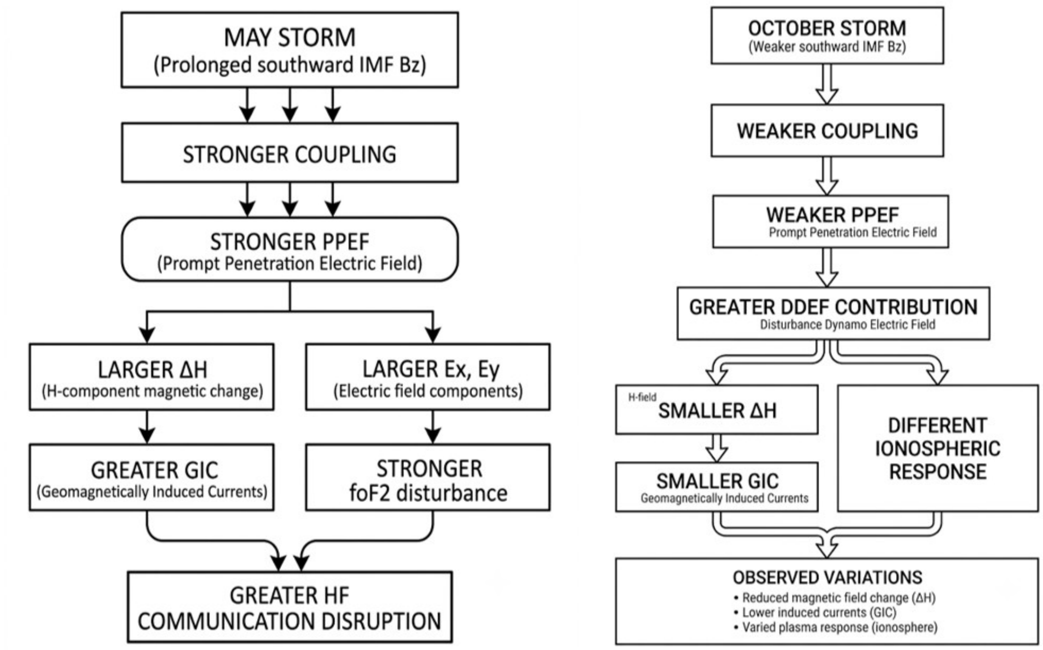

Figure 8. Schematic Illustration of the Different Geomagnetic Field and Ionospheric Responses Over Indonesia Between the May 2024 and October 2024 Storms

from these processes is not possible with the current observations (Astafyeva et al., 2025).

The ionospheric response to the May and October 2024 geomagnetic storms exhibits clear spatial structuring over the Indonesian region, largely controlled by geomagnetic latitude. The contrasting responses observed at PTN and KPG highlight the importance of equatorial and low-latitude electrodynamics in modulating storm-time ionospheric variability. Differences in the timing, magnitude, altitude response, and persistence between the two stations further suggest the combined influence of regional electrodynamics and local time in shaping the ionospheric response to global geomagnetic disturbances.

We acknowledge that Zhang et al. (2024) provided important context on storm-time PPEF behavior across the Asian-Australian and American sectors, demonstrating the utility of ground-based ΔH measurements as a qualitative proxy for daytime PPEF. Huang et al. (2025) further reported multiple nighttime electric field penetration events on 11 May 2024 using incoherent scatter radar, an observational capability currently unavailable in the Indonesian sector. Their results are in line with the persistent ΔH disturbances seen at PTN and KPG at night, which point to ongoing electrodynamic activity during storms over the Indonesian region.

This study highlights the critical role of storm-time electrodynamics in controlling ionospheric variability over equatorial regions. However, a key limitation is the absence of hmF2 analysis, which prevents direct validation of vertical plasma uplift associated with PPEF. Future work should incorporate hmF2 estimation, for example, through ionogram scaling using SAO Explorer, to provide direct observational evidence of vertical ionospheric dynamics.

3.5 Latitudinal Contrast in Electrodynamic Response

A latitudinal contrast framework was used to identify spatial variability in electrodynamic responses during storm periods using PTN, located close to the outer geomagnetic equator, and KPG, located close to the southern crest of the Equatorial Ionization Anomaly (EIA). PTN showed higher and faster ΔH changes during the periods of strong prompt penetration electric field (PPEF) activity. In contrast, KPG usually had weaker and later responses, particularly during the recovery phase when storm-time ionospheric variability remained pronounced. The spatial asymmetry suggests that equatorial intensification is influenced not only by the storm strength but also by local time and background electromagnetism. This feature is demonstrated by the October 2024 storm, which showed spatial diversity in the geomagnetic reaction throughout the Indonesian sector because ΔH minima at PTN and KPG occurred at separate periods. These variations demonstrate how local time and geomagnetic latitude affect storm-time variations seen across Indonesia.

Previous studies on the equator, such as those covering Brazil (Silva et al., 2024) and India (Joshi et al., 2022), have found ΔH increases that correlate positively with the global Dst index and AE index. This shows that low-latitude geomagnetic disturbances tend to exceed global averages. There is a need for geomagnetic instrumentation in particular regions to better define space weather in equatorial regions. This observed pattern is in agreement with the theory for PTN, as the location

Table 3. Comparison of Representative Low-Latitude GIC Studies and the Present Work

Study	Region	Approx. (MLAT)	Major Storm Event	Method	Measured GIC	Main Finding
(Liu et al., 2014)	North China	~ 30°-40° MLAT	29-31 October 2003 (Halloween storm)	Geophysical modeling	~ 60 A	Showed that severe GICs can occur in the Chinese power grid under extreme magnetic storms.
(Barbosa et al., 2015)	Itumbiara, Central Brazil	~ −18° MLAT (geomagnetic)	29-31 October 2003 (Halloween storm)	Geophysical modeling using regional conductivity model	~ 30 A	Showed that significant GICs may occur in low-latitude power systems despite their lower magnetic latitude.
(Abda et al., 2022)	Peninsular Malaysia	~ −2°-8° MLAT	Hypothetical severe storm scenario	Numerical simulation using uniform geoelectric field (1.2 V km^{-1})	~ 44.6-58 A	Showed the strong influence of network topology and transmission-line orientation on GIC distribution.
(Marshall et al., 2013)	Australia	~ −19°- − 30° MLAT	14-15 July 2012 magnetic storm	Measured transformer neutral currents during the 14-15 July 2012 geomagnetic storm.	~ 4-5 A	Showed that even relatively small GICs can affect transformer operation in Australia power systems.
(Watari et al., 2021)	Japanese, Kyushu	~ 20°-30° MLAT	8 September 2017 magnetic storm	Utility assessment and GIC modeling	~ 10 A	Showed that even relatively small GICs can affect transformer operation in Japanese power systems.
(Gonzalez-Esparza et al., 2024)	Three 400-kV Mexican National Power Grid	~ 15°-30° MLAT	10-11 May 2024 (Mother's Day Storm)	Direct GIC measurements using transformer neutral-current sensors	>~ 40 A; ~ 7 A	Showed that significant GICs can occur in relatively low-latitude power systems during the Mother's Day Storm and provided one of the first direct GIC measurements
(Rout et al., 2025)	Indian equatorial sector	~ 0°-15° MLAT	Mother's Day Storm (10-11 May 2024)	Multi-instrument ionospheric observations (GNSS TEC, ISR, Swarm, magnetometers)	Not evaluated	Revealed the dominant roles of PPEFs, enhanced vertical plasma drifts, and EIA evolution during the Mother's Day Storm but did not investigate power systems or GIC.
(Vishnupriya and Manju, 2025)	India, African & American sector	-	30 geomagnetic storms (2002-2024), including Mother's Day Storm	Maximum dB/dt = 95 nT min^{-1} over equatorial India, 154 nT min^{-1} over the American sector, and 120 nT min^{-1} over the African sector.	Not evaluated	Both studies emphasize that low-latitude and equatorial regions are susceptible to conditions favorable for GIC generation during severe geomagnetic storms.
This study	Indonesia (500-kV JAMALI transmission network)	PTN: ≈ −9.30° MLAT; KPG: ≈ −18.37° MLAT	10-11 May 2024 and 10-11 October 2024	First-order geophysical modeling using observed geomagnetic disturbances	0.6-1.6 A	First integrated assessment linking geomagnetic disturbances, ionospheric variability, HF communication impacts, and potential GIC hazards in the Indonesian sector.

close to the geomagnetic equator provides it with a zone of peak PPEF coupling and enhanced equatorial electrodynamic activity (Abadi et al., 2021; Carmo et al., 2024; Paul et al., 2025).

Between KPG and PTN, during the 10 -11 May 2024 ionospheric storm, PTN had a more positive and greater ionospheric response than KPG. These effects are due to the position of PTN and KPG in relation to the geomagnetic equator, which tends to have a stronger electrodynamic influence and fewer effects at higher latitudes within the Equatorial Ionization Anomaly (EIA) (Breber and Hadi, 2024). Moreover, the delayed response at KPG during the period 10-11 October 2024 compared to PTN suggests the delay might be attributed to the composition-driven mechanisms and regional ionospheric dynamics.

This difference also indicates the complicated spatial structure of the equatorial storm time. PTN showed bigger ΔH variations and quicker response times in the ionosphere, suggesting that the eastward PPEF was stronger. On the other hand, KPG had more pronounced and delayed diffusion gap outages that were a result of the storm-time plasma redistribution and EIA modulation. The stronger geomagnetic and ionospheric disturbances observed during the May 2024 storm primarily reflect more efficient solar wind-magnetosphere coupling than during the October 2024 storm. During the May event, the prolonged southward IMF *Bz*, together with elevated solar wind speed and dynamic pressure, enhanced magnetic reconnection at the dayside magnetopause, thereby increasing the transfer of solar wind energy into the magnetosphere. This enhanced energy input intensified the magnetospheric current systems, including the ring current and field-aligned currents, resulting in larger geomagnetic field perturbations (ΔH) observed at both PTN and KPG. Consequently, the stronger temporal variations in the geomagnetic field generated larger geoelectric fields and, therefore, higher estimated GICs than those during the October 2024 storm. A similar contrast is evident in the ionospheric responses to the two geomagnetic. During the May 2024 superstorm, stronger and more persistent PPEF, driven by the enhanced solar wind-magnetosphere coupling, produced larger penetration electric fields and stronger E × B plasma drifts, leading to more pronounced ionospheric disturbances. In contrast, during the October 2024 storm the penetration electric fields were weaker, yet a prolonged negative ionospheric response was still observed, suggesting that storm-time neutral winds and composition changes played a larger role in sustaining the depletion. These results indicate that the contrasting geomagnetic and ionospheric responses between the May and October 2024 storms were controlled not only by differences in storm intensity but also by variations in the efficiency of solar wind-magnetosphere coupling, and by the latitudinal position of each station relative to the magnetic equator and the southern EIA crest.

Beyond their scientific significance, these findings carry important implications for space-weather risk management in Indonesia. The detection of measurable GIC during intense storms demonstrates that Indonesia's expanding high-voltage transmission network is not immune to space-weather impacts, despite its low magnetic latitude. This underscores the importance of implementing targeted GIC risk assessments and real-time monitoring at critical substations along the JAMALI corridor. Previous studies have shown that GIC amplitudes as low as 7 A in 275 kV systems can induce transformer half-cycle saturation and degrade operational performance (Zawawi et al., 2020). As shown in Figure 4, although the maximum estimated GIC in the present study (approximately 1.6 A) is substantially lower than the current levels generally associated with transformer half-cycle saturation and severe operational impacts, it is comparable to the GIC magnitudes reported for other low-latitude power systems. As a practical benchmark for transformer performance under low-latitude conditions, the simulation study of Zawawi et al. (2020) on the Trans-Malaysian transmission network reported that minor effects on transformer neutral operation may begin to occur at GIC levels of approximately 7 A. Relative to this reference value, the maximum GIC estimated for the JAMALI transmission network is approximately 23% of the reported threshold, suggesting a relatively low immediate risk of transformer malfunction during the May and October 2024 geomagnetic storms.

Ionospheric disturbances have been documented with major declines in foF2. These disturbances are problematic for communication systems that use HF radio for aviation and maritime. The findings underscore the importance of functioning space weather alert systems in the equatorial belt that integrate ionospheric observations with geomagnetic and solar wind monitoring to mitigate the impacts of adverse disturbances on communication and other systems. A summary schematic of the solar wind-magnetosphere coupling and subsequent effects during the May and October 2024 storms is shown in Figure 8.

Figure 8 summarizes the physical coupling proposed in this study. Enhanced solar wind forcing, characterized by prolonged southward IMF *Bz*, elevated solar wind speed, and increased dynamic pressure, promotes efficient magnetic reconnection at the dayside magnetopause and intensifies magnetospheric convection. These processes strengthen the ring current, field-aligned currents, and PPEF. To better position the present work within the existing literature, Table 3 compares representative GIC studies conducted in low- and mid-latitude regions. Although previous investigations have demonstrated that geomagnetic storms can generate measurable GICs in low-latitude power systems, most have focused either on GIC modeling or on ionospheric electrodynamics. The present study extends these efforts by integrating geomagnetic observations, ionospheric responses, and first-order GIC modeling within a single framework, thereby providing a comprehensive assessment of space-weather impacts on Indonesia's equatorial power infrastructure and HF communication environment during the two largest geomagnetic storms of Solar Cycle 25.

Isolating the individual contribution of disturbance dynamo electric fields would require direct measurements of equatorial vertical plasma drift, such as incoherent scatter radar or equatorial electrojet estimates, which are not currently available for the Indonesian sector.

4. CONCLUSIONS

The two strongest geomagnetic storms of Solar Cycle 25, on 10-11 May and 10-11 October 2024, demonstrate that Indonesia's equatorial region is not immune to space weather impacts. Combining magnetometer and ionosonde observations at Pontianak (PTN) and Kupang (KPG) with first-order GIC modeling for the 500-kV Java-Madura-Bali (JAMALI) transmission network, we found that local geomagnetic disruptions were exceptionally severe: during the May 2024 storm PTN recorded a ΔH depression of -471 nT, approximately 16% larger than the global Dst minimum of -406 nT, and, being closer to the magnetic equator, responded earlier and more strongly than KPG near the southern EIA crest. The associated geoelectric fields yielded estimated GICs of 0.6-1.6 A along the JAMALI lines, below the levels generally associated with transformer half-cycle saturation yet comparable to those reported for other low-latitude power systems. Both observatories recorded F2-layer depletions exceeding 50%, reducing the high-frequency maximum usable frequency (MUF) by about 4 MHz. These results provide the first integrated assessment of storm-time GIC and ionospheric hazards for the Indonesian sector and underline the need for continuous GIC monitoring and inter-agency coordination to protect national power, aviation, and communication infrastructure.

5. ACKNOWLEDGEMENT

We would like to express our gratitude to the reviewer and also the PICs (Persons in Charge) responsible for providing geomagnetic field data from Pontianak and Kupang. Special thanks are also extended to the PIC at `https://wdc.kugi.kyoto-u.ac.jp/wdc/Sec3.html` for providing Dst data that greatly supported the analysis in this research.

REFERENCES

ITU-R (2019). Method for the Prediction of the Performance of HF Circuits. Recommendation ITU-R P.533-14 P.533-14, Geneva, Switzerland

Aa, E., Y. Chen, and B. Luo (2024). Dynamic Expansion and Merging of the Equatorial Ionization Anomaly During the 10–11 May 2024 Super Geomagnetic Storm. *Remote Sensing*, **16**(22); 1–16

Abadi, P., Y. Otsuka, H. X. Liu, K. Hozumi, D. R. Martinigrum, P. Jamjareegulgarn, L. T. Thanh, and R. Otadoy (2021). Roles of Thermospheric Neutral Wind and Equatorial Electrojet in Pre-Reversal Enhancement, Deduced from Observations in Southeast Asia. *Earth and Planetary Physics*, **5**(5); 387–396

Abda, Z. M. K., N. F. Ab Aziz, Z. A. Rhazali, and M. Z. A. Ab Kadir (2022). Geomagnetically Induced Current Analysis in Malaysian Power Transmission System. *IEEE Access*, **10**; 110205–110216

Ahmad, N., L. O. M. M. Kilowasid, H. Fakhrurroja, Neflia, A. Rachman, A. Husin, and H. Fathoni (2025). How Geomagnetic Storms Affect the Loss of Starlink Satellites in February 2022? *Earth, Planets and Space*, **77**(1); 2

Astafyeva, E., B. Maletckii, M. Förster, I. Ouar, J. Huba, M. Hairston, and W. Coley (2025). Electrodynamic and Ionospheric Puzzles of the 10–11 May 2024 Geomagnetic Superstorm. *Journal of Geophysical Research: Space Physics*, **130**(5); e2024JA033284

Balan, N., L. B. Liu, and H. J. Le (2018). A Brief Review of Equatorial Ionization Anomaly and Ionospheric Irregularities. *Earth and Planetary Physics*, **2**(4); 257–275

Barbosa, C., L. Alves, R. Caraballo, G. A. Hartmann, A. R. Papa, and R. J. Pirjola (2015). Analysis of Geomagnetically Induced Currents at a Low-Latitude Region Over the Solar Cycles 23 and 24: Comparison between Measurements and Calculations. *Journal of Space Weather and Space Climate*, **5**; A35

Bhattacharjee, S., M. N. Shrivastava, U. Pandey, B. Brawar, K. Nanda, S. K. Panda, S. M. Potirakis, S. Sasmal, A. Datta, and A. K. Maurya (2025). Contrasting Low-Latitude Ionospheric Total Electron Content Responses to the 7–8 and 10–11 October 2024 Geomagnetic Storms. *Atmosphere*, **16**(12); 1–20

Boteler, D. (2014). Methodology for Simulation of Geomagnetically Induced Currents in Power Systems. *Journal of Space Weather and Space Climate*, **4**; A21

Boteler, D. H. (2015). The Evolution of Québec Earth Models Used to Model Geomagnetically Induced Currents. *IEEE Transactions on Power Delivery*, **30**(5); 2171–2178

Breber, S. H. and K. A. Hadi (2024). The Impact of Geomagnetic Storms on the Ionospheric Critical Frequency in the Northern and Southern Mid-Latitude Hemisphere Regions. *Iraqi Journal of Science*, **65**(10); 5999–6013

Carmo, C. d. S. d., L. Dai, C. M. Wrasse, D. Barros, H. Takahashi, C. A. O. B. Figueiredo, C. Wang, H. Li, and Z. Liu (2024). Ionospheric Response to the Extreme 2024 Mother's Day Geomagnetic Storm Over the Latin American Sector. *Space Weather*, **22**(12); e2024SW004054

Fejer, B. G., L. A. Navarro, and D. Chakrabarty (2024). Recent Results and Outstanding Questions on the Response of the Electrodynamics of the Low Latitude Ionosphere to Solar Wind and Magnetospheric Disturbances. *Frontiers in Astronomy and Space Sciences*, **11**; 1471140

Gonzalez-Esparza, J. A., E. Sanchez-Garcia, M. Sergeeva, P. Corona-Romero, L. X. Gonzalez-Mendez, J. F. Valdes-Galicia, et al. (2024). The Mother's Day Geomagnetic Storm on 10 May 2024: Aurora Observations and Low-Latitude Space Weather Effects in Mexico. *Space Weather*, **22**; e2024SW004111

Guo, X., B. Zhao, T. Yu, H. Hao, W. Sun, G. Wang, M. He, T. Mao, G. Li, and Z. Ren (2024). East–West Difference in the Ionospheric Response During the Recovery Phase of May 2024 Super Geomagnetic Storm Over East Asia. *Journal of Geophysical Research: Space Physics*, **129**(9); 1–20

Horaites, K., M. Alho, Y. Pfau-Kempf, U. Ganse, A. Workayehu, J. Suni, et al. (2026). Geoelectric Field Caused by Flux Transfer Events in an Ionosphere-Coupled Vlasiator Simulation. *Journal of Geophysical Research: Space Physics*, **131**; e2026JA035175

Huang, C. S., S. Sazykin, J. L. Chau, N. Maruyama, and M. C. Kelley (2007). Penetration Electric Fields: Efficiency and Characteristic Time Scale. *Journal of Atmospheric and Solar-Terrestrial Physics*, **69**(10–11); 1135–1146

Huang, C. S. and Y. Zhang (2021). Equatorial Plasma Drifts During the Magnetic Storm on November 7–11, 2004: Identifications of the Roles of Penetration and Disturbance Dynamo Electric Fields With Multi-Instrumental Measurements. *Journal of Geophysical Research: Space Physics*, **126**(9); 1–25

Huang, F., J. Lei, X. Yue, Z. Li, N. Zhang, Y. Cai, et al. (2025). Interplay of Gravity Waves and Disturbance Electric Fields to the Abnormal Ionospheric Variations During the 11 May 2024 Superstorm. *AGU Advances*, **6**; e2024AV001379

International Electrotechnical Commission (2003). International Standard 60228. Technical Report 60228

Ippolito, A., L. Perrone, C. Plainaki, and C. Cesaroni (2020). Investigating the foF2 Variations at the Ionospheric Observatory of Rome during Different Solar Cycles Minimums and Levels of Geomagnetic Activity. *Journal of Space Weather and Space Climate*, **10**; 52

Joshi, D. R., K. M. Groves, J. M. Retterer, C. S. Carrano, and P. A. Roddy (2022). Peak-Height Distribution of Equatorial Ionospheric Plasma Bubbles: Analysis and Modeling of C/NOFS Satellite Observations. *Journal of Geophysical Research: Space Physics*, **127**(9); 1–17

Kappenman, J. and W. Radasky (2021). Geomagnetic Field Impacts on Ground Systems. *Space Weather Effects and Applications*; 183–213

Laundal, K. M. and A. D. Richmond (2017). Magnetic Coordinate Systems. *Space Science Reviews*, **206**(1); 27–59

Liu, C., Y. Li, and R. Pirjola (2014). Observations and Modeling of GIC in the Chinese Large-Scale High-Voltage Power Networks. *Journal of Space Weather and Space Climate*, **4**; A03

Loewe, C. A. and G. W. Prölss (1997). Classification and Mean Behavior of Magnetic Storms. *Journal of Geophysical Research*, **102**(A7); 14209–14213

Love, J. J., H. Hayakawa, and E. W. Cliver (2019). Intensity and Impact of the New York Railroad Superstorm of May 1921. *Space Weather*, **17**(8); 1281–1292

Marshall, R. A., H. Gorniak, T. Van Der Walt, C. L. Waters, M. D. Sciffer, M. Miller, M. Dalzell, T. Daly, G. Pouferis, G. Hesse, and P. Wilkinson (2013). Observations of Geomagnetically Induced Currents in the Australian Power Network. *Space Weather*, **11**(1); 6–16

Moges, S. T., N. M. Giday, D. A. Chekole, T. Ulich, and R. O. Sherstyukov (2022). Storm-Time Observations of Traveling Ionospheric Disturbances and Ionospheric Irregularities in East Africa. *Radio Science*, **57**; e2022RS007426

Nayak, C., S. Buchert, E. Yiğit, M. Ankita, S. Singh, S. Tulasi Ram, and A. P. Dimri (2025). Topside Low-Latitude Ionospheric Response to the 10–11 May 2024 Super Geomagnetic Storm as Observed by Swarm: The Strongest Storm-Time Super-Fountain During the Swarm Era? *Journal of Geophysical Research: Space Physics*, **130**(3); e2024JA033340

Paul, K. S., M. Moses, H. Haralambous, and C. Oikonomou (2025). Effects of the Mother's Day Superstorm (10–11 May 2024) over the Global Ionosphere. *Remote Sensing*, **17**(5); 1–24

Rout, D., A. Kumar, R. Singh, S. Patra, D. K. Karan, S. Chakraborty, et al. (2025). Evidence of Unusually Strong Equatorial Ionization Anomaly at Three Local Time Sectors During the Mother's Day Geomagnetic Storm on 10–11 May 2024. *Geophysical Research Letters*, **52**; e2024GL111269

Santoso, A., S. Sismanto, R. Priyatikanto, E. Hartantyo, E. S. Mumpuni, L. O. M. M. Kilowasid, A. Rachman, F. Nuraeni, S. Filawati, Erlansyah, and D. Nurmali (2025). Assessment of the Severe Geomagnetic Storm on May 10–11, 2024 Effects on the Geomagnetic Field and Ionosphere over the Indonesian Region. *Rudarsko-Geološko-Naftni Zbornik*, **40**(4); 125–136

Shreedevi, P., A. S. Nair, Y. Miyoshi, S. C. Buchert, Y. Otsuka, A. Shinbori, L. G. Krishnan, S. Perwitasari, and M. Nishioka (2025). Superstorm-Driven Electron Temperature (T_e) Anomalies in the Topside Low-Latitude Ionosphere: Role of the Equatorial Ionization Anomaly (EIA). *Earth, Planets and Space*, **77**(1); 163

Silva, G. B. D. d., L. R. Alves, K. Espinosa, V. Souza, L. da Silva, J. Costa, M. Pádua, and S. Sanchez (2024). Evaluation of dB/dt Amplitudes and Sources Over the Brazilian Region during Geomagnetic Storms in the 2021–2022 Biennium. *Journal of Atmospheric and Solar-Terrestrial Physics*, **258**; 106196

Tulasi Ram, S., B. Veenadhari, A. Dimri, J. Bulusu, M. Bagiya, S. Gurubaran, N. Parihar, B. Remya, G. Seemala, R. Singh, et al. (2024). Super-Intense Geomagnetic Storm on 10–11 May 2024: Possible Mechanisms and Impacts. *Space Weather*, **22**(12); e2024SW004126

Vishnupriya, K. S. and G. Manju (2025). Risk Assessment of Geomagnetically Induced Currents (GICs) over the Indian Sector in Comparison with American and African Sectors. *Space Weather*, **23**; e2024SW004133

Watari, S., S. Nakamura, and Y. Ebihara (2021). Measurement of Geomagnetically Induced Current (GIC) Around Tokyo, Japan. *Earth, Planets and Space*, **73**(1); 102

Zawawi, A. A., N. F. A. Aziz, M. Z. A. A. Kadir, H. Hashim, and Z. Mohammed (2020). Evaluation of Geomagnetic Induced Current on 275 kV Power Transformer for a Reliable and Sustainable Power System Operation in Malaysia. *Sustainability*, **12**(21); 1–23

Zhang, X., W. Kong, N. Yu, H. Chen, T. Li, and E. Wang (2024). Comparison of Different Geoelectric Field Methods to Calculate Geomagnetically Induced Currents in North China. *International Journal of Electrical Power & Energy Systems*, **155**; 109657

